Feasibility of Supersonic Retropropulsion Based on Assessment of Mars-Relevant Flight Data

Brandon Sforzo*
Georgia Institute of Technology, Atlanta, GA 30332
Robert D. Braun†
University of Colorado at Boulder, Boulder, CO, 80309

Flight data provided by SpaceX for flights was analyzed to demonstrate the applicability of telemetry during SRP to Mars relevant conditions. This information was provided under the framework of a public-private partnership with NASA, executed as a Space Act Agreement. Analysis focused on the entry burn portion of the trajectory. Flight conditions were provided to confirm SRP occurred during an applicable range of mach numbers and dynamic pressures to match Mars SRP initiation conditions. Vehicle trajectory and attitude history were provided for the SRP segment as well as onboard sensors for temperature, pressure, heat flux, and strains to compare between missions. Furthermore, NASA airborne assets provided thermal imagery of the first stage during SRP to provide comparison to onboard data. Plume tracking analysis was compared to dynamic data from sensors with little correlation. Analysis of these onboard sensor data and examination of the details for several missions, the performance of the Falcon 9 vehicle during SRP appeared to be well behaved for these flights. This study illustrates that SRP methodology implemented for the Falcon 9 first stage entry does not adversely affect the vehicle and shows promise for future implementation.

I. Introduction

SRP has been identified as an enabling technology for future robotic and manned Mars missions with large payloads. Parametric studies predict the applicability of SRP to landing payloads ranging from 1.5 metric tons (t) to greater than 5 t. Additional benefits of SRP include desirable control authority through thrust vectoring and throttling and scalability through the range of payloads, offering cost benefits. The technology gap between current Mars landing capabilities of approximately 1 t and future large missions requires a progression of demonstrative ground tests, flight tests, and simulations in order to mature SRP for incorporation into future system designs. Identified gaps in the current understanding relate to the effects of directing propellant against the supersonic freestream. This yields complicated flowfields due to the interactions of the exhaust plume and shocks, which may also impinge on the vehicle body. Technical risks associated with SRP include aerothermodynamic interactions, engine startup challenges, and transitions to steady-state conditions. Understanding these phenomena requires evaluations of operation at flight-relevant conditions. Prior to initiation of this project, small-scale, air-in-air testing was the highest fidelity simulation of supersonic retropropulsion technology. In late 2013, SpaceX successfully demonstrated the operation of a supersonic retropropulsive capability during the re-entry of the first stage of their Falcon 9 launch system. Flight data provided by SpaceX for flights was analyzed to demonstrate the applicability of telemetry during SRP to Mars relevant conditions. Portions of the entry burn segment fell within a range of mach number and dynamic pressures that match Mars SRP initiation conditions. Engine thrust vectoring commands and responses were also analyzed and compared against attitude rates during engine startup and SRP. These assessments highlighted that the Falcon 9 implementation appears to be robust, which has since been further validated by the successful operational flight performance achieved by Falcon 9 first stages. Each of the entry vehicles were outfitted with temperature and heat flux transducers to observe the effects of aerothermal heating. Through trajectory reconstruction, the relative orientation of the vehicle to the opposing flow was compared to these heating trends. Upon SRP initiation, heat fluxes rise as a result of the high enthalpy rocket plume interacting with the surface of the first stage vehicle. The locations of higher heating rates also correlated well with the stagnation point of the incoming flow, as determined by the trajectory reconstruction. This orientation to the flow was also confirmed by external pressure and temperature transducers. Fourier transform analysis was also performed on high speed transducers to detect dynamic effects, particularly at engine start up for SRP. Engine combustion chamber pressures showed negligible dynamic response upon engine startup, within the Nyquist spectral range available. Additionally, high speed strain gauge responses were recorded and showed low amplitude low frequency

*Postdoctoral Fellow, Aerospace Engineering, AIAA Senior Member, brandon.sforzo@gatech.edu
†Dean of Engineering and Applied Science, AIAA Fellow, bobby.braun@colorado.edu

response during SRP, which are typical. The nominal results observed from the detailed analysis of abundant vehicle sensor data supports applicability of SRP at Mars relevant conditions. Comparable trends and heating values between flights also supports the repeatability of these effects. Also, the absence of dynamic response during SRP engine start is a promising experimental result for the stability of this maneuver.

II. Data Sources

For each SpaceX Falcon 9 mission, a set of data files were provided, containing guidance navigation and control (GNC), atmospheric wind data (Wind) and predictions, and vehicle sensor data (Aero). The two missions examined here are listed with information in Table 1. Specifically, the missions are labeled "F9-#" for the Falcon 9 booster used and the mission number of the rocket. The main payload for that mission is also listed, with the launch date and approximate launch time. The launch site for both is Cape Canaveral Air Force Station Space Launch Complex 40 (CC SLC-40). Additionally, listed in the table, are the mission times (time from launch) for the beginning of the SRP event, the end of SRP, and the event duration. Table 1 also details which mission had a booster outfitted with landing legs.

All data provided were processed by SpaceX and have been downsampled to a common $50\,Hz$ for comparison. Specific data streams were further analyzed from their raw sources in the native sampling frequency.

Table 1. Details of SpaceX Falcon 9 missions that supplied data to NASA. Approximate timing information on the SRP portion of each flight is provided for the start ($t_{SRP,i}$) and finish ($t_{SRP,f}$) of the event, following launch. The total SRP duration is provided by τ_{SRP} entries.

	F9-10	**F9-13**
Payload	Orbcomm	CRS-4
Date	7/14/2014	9/21/2014
Time (UTC)	15:15	5:52:03
Site	CC SLC-40	CC SLC-40
$t_{SRP,i}$	510	440
$t_{SRP,f}$	550	460
τ_{SRP}	40	20
Ldg. Legs	Yes	No

A. GNC Data

The Guidance Navigation and Control data provided vehicle information through the mission, including engine conditions, operating state, and attitude.

The engine combustion chamber pressures were used, in part, to determine the various stages of the mission. The pressure histories during the SRP phase of flight for each engine are plotted together for the two separate missions, and can be seen in Fig 1, as normalized by the "full throttle" pressure. As can be seen in the plot, the entry burn (SRP) lasts about $20 - 40\,s$.

B. Wind Data

The Wind data primarily contains conditions that the vehicle experiences throughout the mission. The atmospheric conditions that are used for these variables come from a variety of measurement and simulated sources. Many of the variables incorporate modeled atmospheric range conditions, including the wind velocity, in the vehicle trajectory. The data provided for the position and direction of the vehicle are derived from guidance sensor data to reconstruct the best estimated trajectory (BET).

C. Aero Data

Aerothermal sensor data from the Falcon 9 vehicle were provided in the Aero file for each mission. This data file nominally included a structure variable containing "raw" data, and separate structure variables containing "reduced" data streams for stage 1 and stage 2 transducers.

All of the "reduced" data was downsampled from the native sampling frequency, which ranged from 10's of Hz (indicated subsequently as "low frequency") to multi-kHz. The low frequency data was the most comparable between data streams and missions, and was used for the majority of analysis.

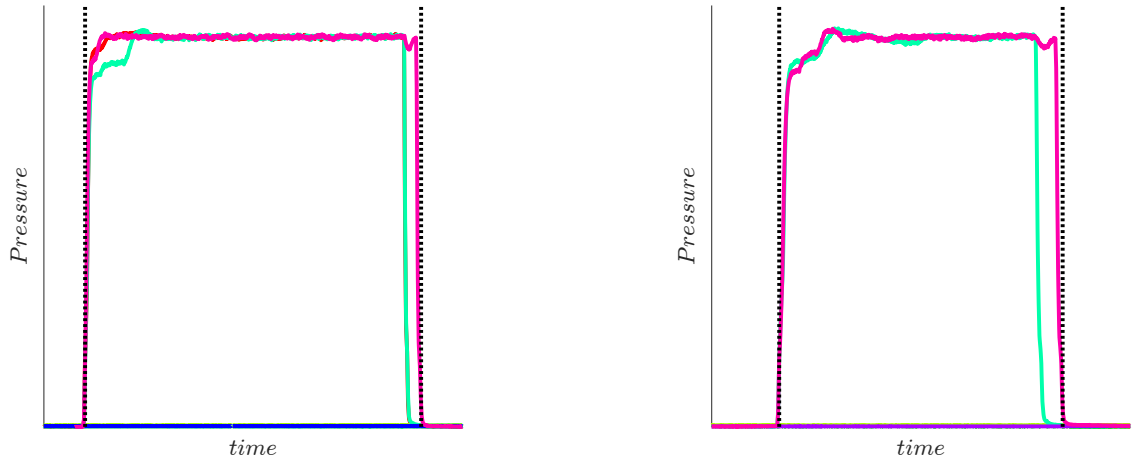

a) F9-10 **b) F9-13**

Figure 1. Engine chamber pressures for each mission, during the SRP phase of the trajectory. Nominally, only engines 1, 5, and 9 are commanded to operate during this entry burn.

1. Sensor Locations

Sensor data was provided for many transducer locations on the vehicle. Sensors located on the base of the vehicle were well suited for comparison between missions and sensor types for the SRP regime. The radial locations of these sensors can be seen in Fig. 2. Each of the sensors on the base of the vehicle is in located azimuthally in reference to one of the nine engines and radially to one of three concentric rings. The outer most ring ("Outer") is located at a radius outside the radial position of the engines with eight sensor locations provided. The next inner ring ("Inner") is located within the ring of engines, with eight locations provided. The last grouping of sensors is located on the engine 9 heat shield ("E9") at a radial distance from the axis of the vehicle with four sensor locations provided. The line style convention used for sensor locations in this figure is maintained in the comparative graphs in this chapter, denoting radial location.

2. Vehicle Pressures

The database provided contained several pressure transducer streams from internal components. The relevant parameter for this investigation were the engine chamber pressures, supplied with the same time steps as the remainder of the aero data set. Additionally, the raw data from this stream was also examined at its native milti-kHz sampling.

3. External Pressures

External pressures on the vehicle were measured in several groupings where the naming convention for each of these sensors is organized by which engine they are located by. They are arranged in rings, as described above. Data was provided at low frequency sampling.

4. External Temperatures

Thermocouple temperature data streams were provided from sensors located in the ring arrangement according to Fig. 2. Flight F9-10 has a comprehensive set of sensors in these placements. These data were recorded at the low frequency sampling rate.

5. Calorimeters

Calorimeter measurements were made based on thermocouple readings attached to calibrated copper slugs. The sensors were located according to the mapping in Fig. 2. These readings are provided in units of degree Fahrenheit and required conversion to heat flux as according to Eq.1, where, ρ is the density of copper, t is the thickness of the copper slug, c_p is the specific heat capacity of copper, and $\frac{dT}{dt}$ is the instantaneous rate of change of temperature. The radiative

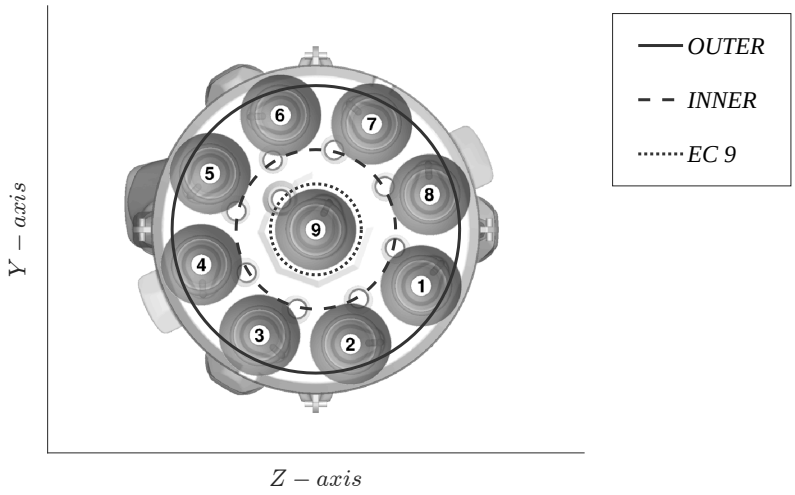

Figure 2. Radial positions, and naming convention for sensors located on the base of the vehicle.

portion of the equation uses the Stefan-Boltzmann constant ($\sigma = 5.67 \times 10^{-}8\ \frac{W}{m^2K^4}$), and an emissivity appropriate for copper, where T is the temperature of the slug as measured by the thermocouple.The slugs used for the calorimeters all had a standard thickness.

$$\dot{q} = \rho * l * c_p * \frac{dT}{dt} + \sigma * \epsilon * T^4 \tag{1}$$

6. Strain

Strain gauges were located on each of the two TVC actuators of certain engines for each of the missions. Strain data were provided with the prepared set of sensor variables at the common low sampling frequency. The high frequency data were used for dynamic vibration analysis.

D. Thermal Imagery

In concert with the F9-13 launch, two airborne assets were deployed to capture thermal imagery of the Falcon 9 first stage trajectory. For this work, the thermal imagery from SRP is analyzed for dynamic trends which may influence or be detected by onboard sensors. The two aircraft, pictured in Fig. 3, were a U.S. Navy NP-3D Orion and a NASA high altitude WB-57. The P-3 aircraft which was equipped with the Cast Glance system and the WB-57 included equipment for visible ($0.4\,\mu m$ to $0.7\,\mu m$) and midwave infrared (MWIR) ($3.4\,\mu m$ to $4.9\,\mu m$) detection. The Cast Glance MWIR imagery was provided in 512×640 resolution at $60\,fps$, whereas the WB-57 imagery was provided in 784×1344 resolution at $30\,fps$. Additional details of the aircraft mission and equipment are available in the companion publication [1].

III. SRP Condition Relevance

The trajectory information, combined with the winds and atmospheric conditions also provide the necessary values for the Mach number of the vehicle and the dynamic pressure that is experienced. These values are appropriate parameters for comparison to Mars entry conditions in order to determine mission relevance. The Mach number and dynamic pressure have been plotted together in Fig. 4 for each mission during the SRP phase.

The entry burn condition begins at the top left corner of each plot and proceeds downward to the right as the Mach number decreases. Simultaneously, the retropropulsion causes deceleration while the vehicle is descending in altitude.

Figure 3. U.S. Navy NP-3D Cast Glance aircraft (L); NASA WB-57 (R).

The dynamic pressure rises initially as the vehicle reaches higher density conditions. The boxed region denotes the powered descent startup conditions at Mars as identified by the EDL-SA project team for human [2] and robotic [3] landed payloads. It is clear from the plot that F9-10 has portions of the propulsive stages in the relevant regime. The F9-13 mission included a "boostback" phase and therefore had a different trajectory from F9-10. This conditional contrast (as seen in Fig. 4) was considered when comparing the telemetry between missions.

IV. Combustion Chamber Pressures

The focus of this report is on the entry burn phase of each of the missions, which is when supersonic retropropulsion occurs. The objective of this assessment was to study data from the missions, and compare trends between missions for common data streams. As was noted previously, the SRP phase was identified by the chamber pressures of engines 1, 5, and 9 of Fig. 1. Here, the engine chamber pressures of just the SRP phase of the mission can be compared. In both cases, the SRP segment lasts between approximately 20 and 40 s, as is listed in Table 1. For the engine pressure traces, the values rise very rapidly and come to a steady state value in 5 s.

The engine pressures were processed at a sampling rate that coincided with the other data for ease of comparison. The raw data was also provided and allowed investigation into any dynamic features in the engine pressures. High speed data were analyzed for engine 9, as this was the common data stream for all missions. Spectral analysis was performed for the SRP portion of the data via a fast Fourier transform (FFT) method. The data was sampled in multi-second intervals and transformed, revealing the overlapping power spectra in Fig. 5 for each mission. The several overlapped signals in each subplot are the several sample segments of the SRP signal.

The amplitude offset of the spectra reveal the increased pressure during the SRP portion. The spectra are relatively flat, suggesting that the dominant signal captured by the transducer is random noise, with no strong tones. The spectra for F9-10 (Fig. 5a) show a slight rise in signal strength for two frequency bands, but these relative rises are not considered significant.

V. Vehicle Attitude

The attitude and attitude rates were plotted for the SRP portion of each mission and can be seen in Fig. 6. The attitudes for F9-10 all show a brief period where the pitch and yaw angles vary, then return to constant values. Slight oscillations in pitch are also observed in this initial transient for both flights, though the rates are below magnitudes that warrant any concern. The initial transient at engine startup is reflected in all the rates, where the pitch and yaw rates remain very manageable at all times for flight F9-10. The greatest variation in attitude for these flights is in the roll component, but the rate remains low as well.

Flight F9-13, overall, shows higher variations in attitude. When observing the trajectory reconstruction, the vehicle experiences a brief pitching adjustment that is to be expected given engine initiation, while, similar to F9-10, the rolling rate continued throughout the maneuver, though not influential to the overall performance of the vehicle.

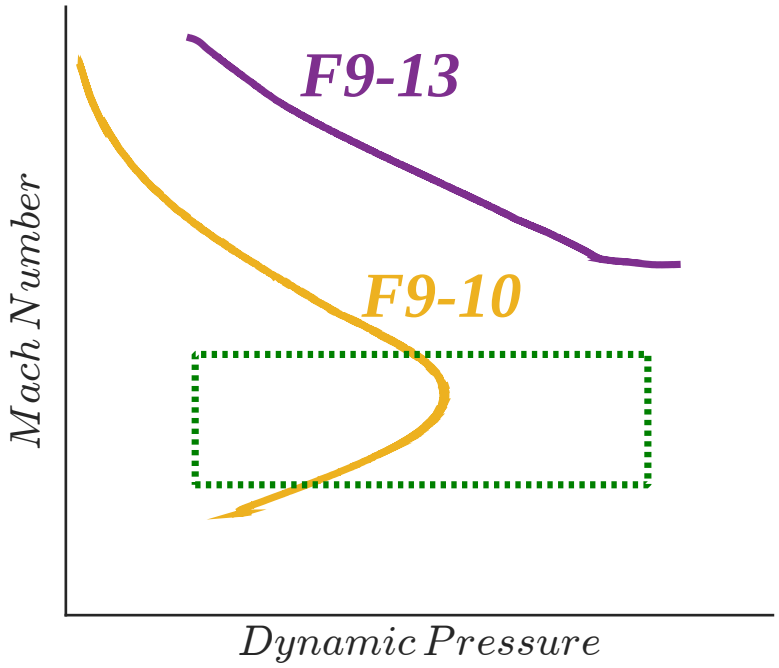

Figure 4. Flight conditions (Mach number and dynamic pressure) during the SRP entry burn phase. The dashed box represents the expected conditions for Mars entry burn initiation from NASA Mars human architecture assessments.

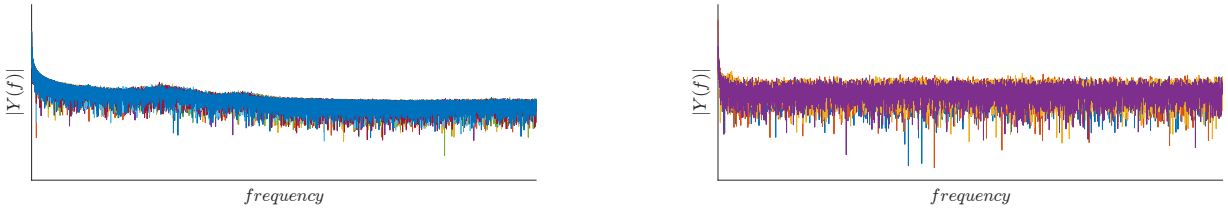

a) F9-10 b) F9-13

Figure 5. Engine 9 chamber pressure spectra during SRP. FFT was performed multi-second signal lengths for the SRP phase. The overlapping spectra in each plot are for each analyzed segment.

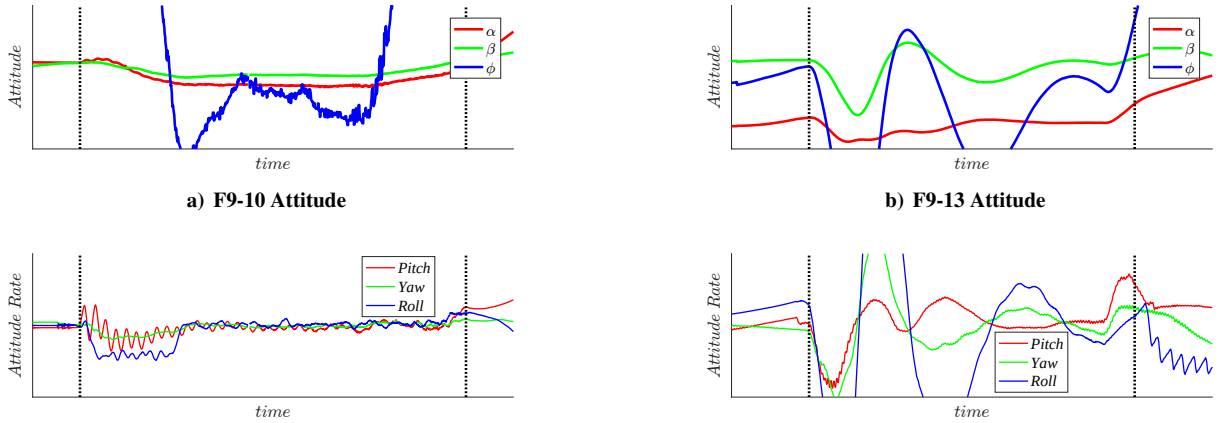

a) F9-10 Attitude b) F9-13 Attitude

c) F9-10 Rates d) F9-13 Rates

Figure 6. Attitude and corresponding attitude rate histories during the SRP portions of each flight. The attitude streams plotted are α (pitch), β (yaw), and ϕ (roll).

VI. Measurement Comparisons

This section compares the onboard sensor data between the four missions. General observations about the trends seen in individual mission data sets are also discussed.

A. Base Pressures

Base pressure measurements were analyzed from the low frequency sampling sensors, as well as downsampled data streams from high frequency sampling sensors, which provided a full sensor sets between missions.

The outer transducer signals, seen in Fig. 7a have four sensor locations displayed with similar behavior between them. During SRP the pressures at these outer locations rise and remain constant throughout the engine burn. The inner pressure transducer signals rise at the start of SRP, with engine 4 showing the largest increase. Based on these measurements, the pressure is likely highest near the inner region on the base of the vehicle, corresponding to where the stagnation point of the flow would fall.

The pressure profiles from the base sensors of F9-13 show more variations, as seen in Fig. 8a for the outer ring of pressure sensors. At the onset of SRP, the pressures rise for the four sensors, as expected due to the exhaust flow. Pressure for the engine 8 sensor rises for a brief period after engine startup and then falls, which can be explained by the attitude changes observed in Fig. 6b. Engine 4 and 6 pressures remain relatively constant during SRP, similar to those in F9-10. These signal behaviors are mirrored in the inner sensor histories in Fig. 8b. Pressure values after completion of the SRP maneuver for the two missions are consistent with overall dynamic pressure trends illustrated in Fig. 4.

B. Base Temperatures

Base temperatures were analyzed for thermocouples located in the three sensor ring locations for mission F9-10 (Fig. 9). For the mission, all sensors data are plotted on the same axes and denoted by their color and line type

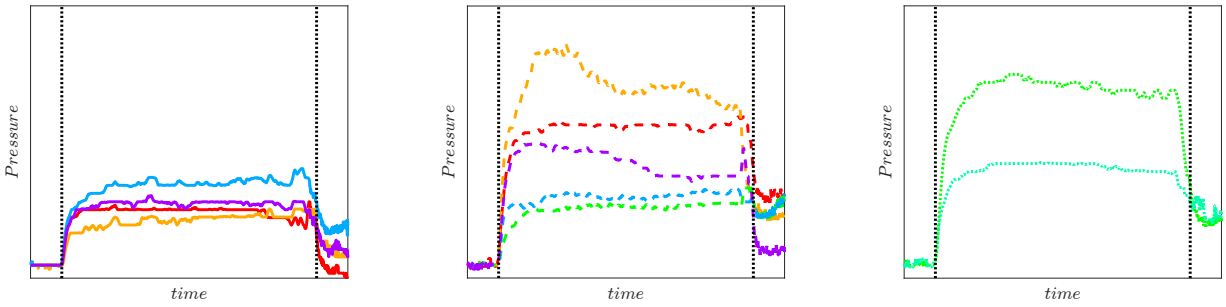

a) Outer b) Inner c) EC 9

Figure 7. Base pressure sensor histories from F9-10 during the SRP segment of the mission (vertical lines). The plots are from the three rings of sensor locations and each line color corresponds to the engine location as depicted in Fig. 2.

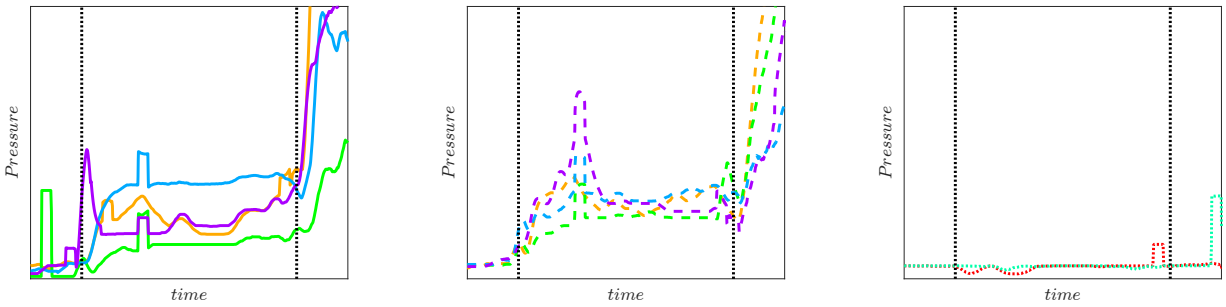

a) Outer b) Inner c) EC 9

Figure 8. Base pressure sensor histories from F9-13 during the SRP segment of the mission (vertical lines). Each line color corresponds to the engine location as depicted in Fig. 2.

according to Fig. 2. The temperature scale is consistent between the three subplots for the different rings of sensors.

Temperature readings prior to SRP for mission F9-10 spanned similar ranges for all sensors plotted, remaining at levels consistent with information provided by heat flux based sensors. These temperatures increased in a manner consistent with an increase in surface heating due to the engine plumes. The low overall temperatures for this mission may be a result of the lower Mach number and dynamic pressure throughout most of the SRP phase of flight.

C. Heat Flux

Heat fluxes were analyzed through calorimeter data as calculated through thermocouple measurements (described in above). These histories are shown in Fig. 10, for mission F9-10. The values for each sensor were zeroed at the onset of SRP to track the relative heat flux through the flight segment.

Readings for flight F9-10 show a rise in heat flux starting at the onset of SRP, with closely located sensors trending similarly. Furthermore, the inner ring of calorimeters exhibit the largest variation in readings, indicating larger variation in surface heating effects which are potentially dependent on the vehicles angle of attack. The sensors located nearest to engine 9 exhibit readings consistent with the other two annular positions.

D. Strain

Strain measurements from gauges mounted on engine thrust vector control actuators were analyzed for the four flights. The histories of these transducers are shown in Fig. 11. The signals were not zeroed or smoothed in order to preserve dynamic behavior.

Flight F9-10 strain readings during SRP are shown in Fig. 11a. The deflection for all struts occurred at the onset of SRP and ended just before the end of the segment. The actuator strain readings associated with engines 1, 5, and 9 demonstrate deflections consistent with these engines being operational during the SRP maneuver.

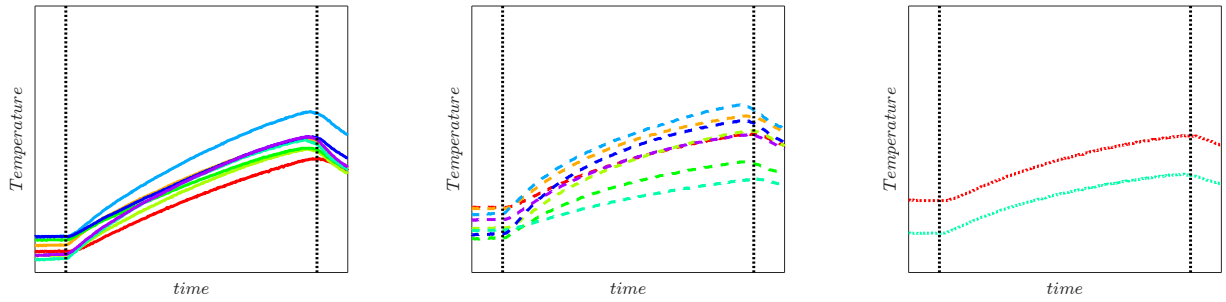

a) Outer **b) Inner** **c) Engine 9**

Figure 9. Base temperature readings during SRP for F9-10. Line types correspond to the sensor radial locations as illustrated in Fig. 2.

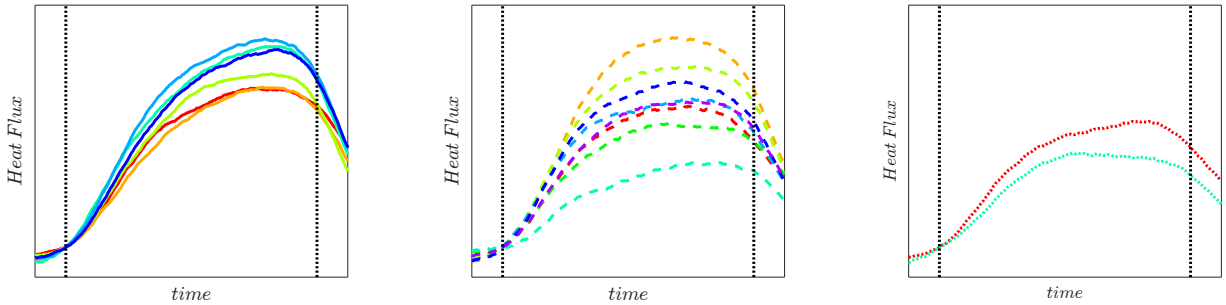

a) Outer **b) Inner** **c) EC 9**

Figure 10. Calorimeter histories during SRP segments of flight (black lines) for F9-10. Sensor locations are coded by color and line style as illustrated in Fig. 2.

The period of varying strain in the engine actuator struts indicated in Fig. 11a & 11b correlates well with the change in vehicle attitude that occurs at the initiation of SRP.

Dynamic information from the strain gauges were also analyzed by taking the Fourier transform of the raw signal. For each mission, the SRP portion of one actuator strain gauge was analyzed by taking multi-second signal lengths and averaging 5 consecutive spectra as an ensemble data set. The resulting sets of spectra are presented in Fig. 12 for both flights.

Throughout SRP, as seen in Fig. 12a, a dominant tone is indicated in the lower frequency band. A similar tone is indicated in one spectra included in Fig. 12b. In addition, there is a portion of spectral energy distributed around a broad higher frequency band near the middle of the frequency range depicted. Although of interest from a pure sense of spectral evaluations, nothing of significance can be attributed to the lower frequency tone or the broader energy spectra seen in Fig. 12a. The essentially flat spectra seen in all but one spectra illustrated in Fig. 12b simply indicates broadband noise.

VII. Plume Dynamics

Data gathered from the imagery aircraft were used to compare against onboard sensor readings for the SRP portion of the mission. Due to the intensity of the emission from the first stage engines and plume, the captured signal was saturated and could not provide quantitative values for the thermal properties of the plume or vehicle during engine on conditions.

The image sequences from both the P-3 (Cast Glance) and the WB-57 (SCIFLI) aircraft were post-processed to reduce noise and correct for vehicle tracking challenges from the acquisition. Background subtraction and median filtering was applied to remove the noise floor of each image. Due to the saturation of the sensors from the intense emission, the image was easily binarized using an intensity threshold. This binary image was used to obtain the orientation of the plume path and also isolate the front edge, where the vehicle exists. A maximum inscribed circle was calculated on the front edge of the plume to determine the vehicle location and then transform the image for

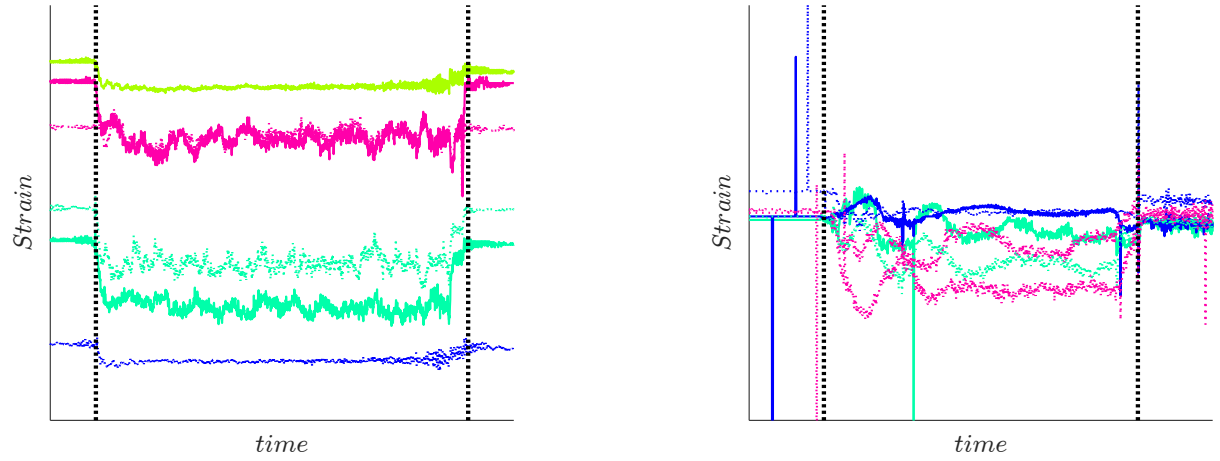

a) F9-10 b) F9-13

Figure 11. Strain gauge readings from both (solid and dashed) thrust vector control actuators, color coded by engine as referenced in Fig. 2.

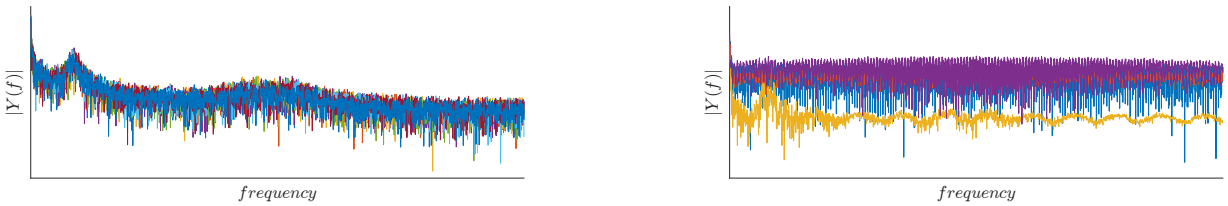

a) F9-10 b) F9-13

Figure 12. Engine 5 support strut strain spectra.

stabilization. An example of a stabilized image with the vehicle centered is seen in Fig. 13, where the stabilization is applied to the original grayscale image.

The plume dynamics were examined based on the waveform appearance of the plume edge tracked in time during the SRP portion of flight. This was extracted using the eccentricity of the plume shape and overlaying a perpendicular line on the trailing plume a fixed distance from the vehicle. The intensity of the signal along the line was gathered and can be seen in Fig. 13b. A threshold was set along this plume intensity line to track the edge of the plume, of which the time series of from the two image sources can be seen in the top plots of Fig. 14. Gaps can be observed in the time series from the WB-57 imagery due to panning of the camera causing the vehicle to momentarilly dip out of frame.

A Fast Fourier Transform (FFT) was performed on these timeseries for constant multi-second periods and the spectra are presented in the bottom plots of Fig. 14. Due to the framerate of the P-3 and the WB-57 cameras, the Nyquist frequencies were 15 Hz and 30 Hz, respectively. This spectral range unfortunately limits the ability to extract potential hydrodynamic fluctuations in the plume. As can be seen in the bottom two subfigures of Fig. 14, no tonal signals are observed in the spectra from the plume edge tracking. Neither the dynamic signals demonstrated in the actuator strut strain gauges at a lower frequency range nor the broader band spectra seen at a moderate frequency appear in the P-3 or WB-57 imagery.

VIII. Discussion

Telemetry data for two Falcon 9 missions were analyzed to observe vehicle behavior during the supersonic retro-propulsive deceleration portion of the mission. These missions were selected due to the relevant dynamic pressures and mach numbers experienced during this maneuver which closely match the conditions required for future missions to Mars, and the available thermal imagery which was acquired for comparison for flight F9-13. These conditions, and other relevant mission information were derived from guidance, navigation, and control data provided by SpaceX for each flight. Vehicle attitude was tracked from the GNC data to provide information on the entry orientation of the

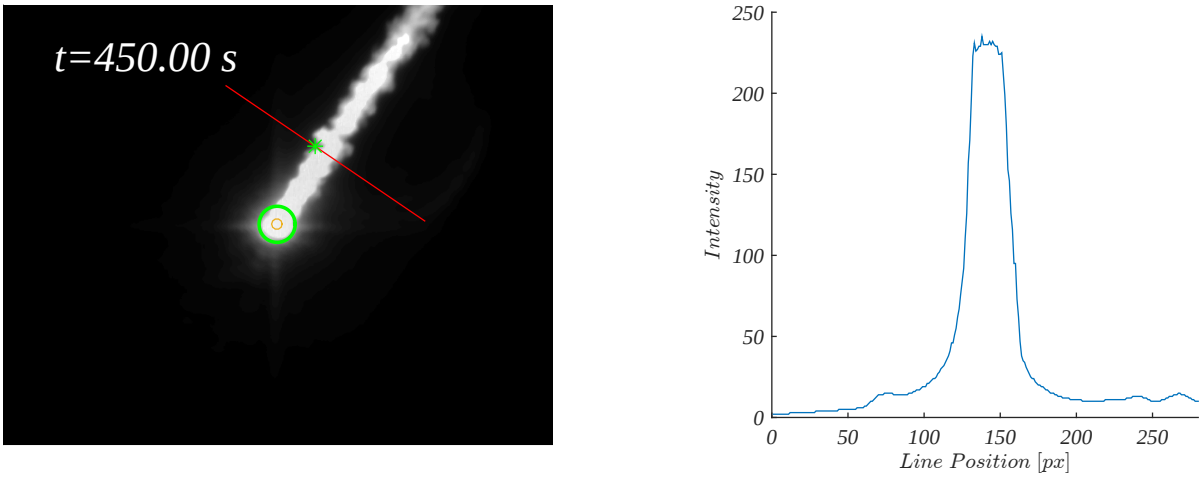

Figure 13. Plume of F9-13 tracked during the SRP with the cross section of the signal intensity used to extract dynamic signal.

vehicle and positional fluctuations during SRP. Additionally, atmospheric and relative wind conditions were used to calculate aerodynamic values.

The SRP portion of the flight was also determined from these data based on the engine chamber pressures, which was used to direct the analysis of the sensor data. The engine chamber pressures during SRP indicated active engines 1, 5, and 9. Engine chamber pressure data sampled at fast rates were analyzed for dynamic signal, with nothing of significance to indicate particular challenges for general SRP applications.

Transducer data were also provided, which included external vehicle pressures, temperatures, heat flux, and strain gauge readings. Base pressures showed similar trends across all missions examined which typically included an increase and sustainment of pressure throughout SRP with the highest observed pressures being closest to the center of the vehicle base. Flight F9-13 showed greater variability in this measurement, which correlates well to the variability in attitude of the vehicle.

Thermocouple data showed similar trends within locations from the F9-10 mission, where the temperature steadily rose from the onset of SRP. These corresponded well with heat flux measurements which were recorded via metallic slug calorimeters. The calorimeters showed a gradual rise in heat flux as SRP proceeded, with the maximum values occurring right before engine shutdown. Since response transients for slug calorimeters are affected by the time constant of the specific measurement device, inclusion of the thermal mass in a calibrated calorimeter model is important in the reduction of measurement response data. For these data, the heat flux magnitudes were derived with a fixed calorimeter wall thickness provided by SpaceX that corresponds to the design of their measurement devices.

Lastly, strain measurements were gathered and analyzed for gauges located on multiple thrust vector control actuators at several engine locations. For both flights, engine actuator deflections were consistent with the utilization of thrust vector control for maintaining the desired vehicle attitude during the SRP maneuver. Mission F9-13 experienced data dropouts that are not unusual for flight vehicles. These data dropouts may also have influenced the dynamic spectra characteristics derived from the timeseries. Spectral investigations using a Fourier transform of multi-second sample lengths with an averaging of five consecutive spectra were performed. These results indicated a lower frequency tone for most individual spectra across the two missions investigated. The lower frequency range of this tone and repeatability across several flights would be consistent with this being due to a vehicle natural frequency or primary structural dynamics mode. Large dynamics or indications of flow or rocket engine flow instabilities, which would increase SRP risk, were not observed during engine startup or in any of the dynamic data analysis during the SRP maneuver.

Following the analysis of these onboard sensor data and examining the details for several missions, the performance of the Falcon 9 vehicle during SRP appeared to be well behaved for these flights. This observation is further substantiated by the achievement of an operational reusable Falcon 9 first stage capability by SpaceX since the time of the flights examined herein. Some contrasts were observed between F9-10 and F9-13, mainly associated with the higher pitch and roll rate that was observed in the vehicle attitude history of F9-13. The vehicles were well outfitted with sensors that compared well with each other and did not exhibit any showstoppers for the SRP technology. Based on this set of data at Mars relevant conditions, it appears that the SRP methodology implemented for the Falcon 9 first

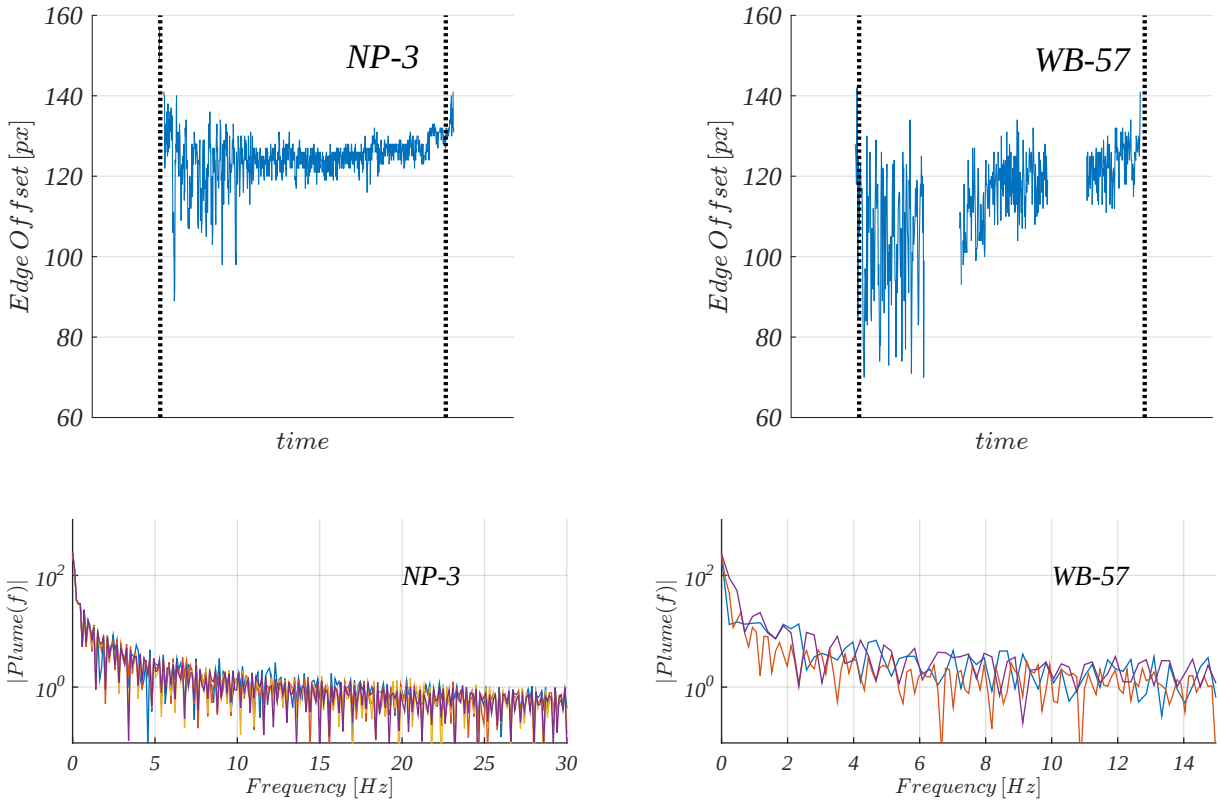

Figure 14. Plume of F9-13 tracked during the SRP with the cross section of the signal intensity used to extract dynamic signal.

stage does not adversely affect the flight vehicle and has promise for additional investigation and further implementation. Of particular interest to NASA in this direction is the utilization of SRP as an enabling capability for Mars human surface missions.

Acknowledgments

This work was funded by the National Aeronautics and Space Administration (NASA) Space Technology Mission Directorate through the Game Changing Development Program's Propulsive Descent Technology project. Data was exchanged between NASA and the Space Exploration Technologies Corp. (SpaceX) through the NRSAA partnership Umbrella NRSAA-EA-14-18828. Any opinions, findings, and conclusions or recommendations expressed in this material are those of the authors and do not necessarily reflect the views of NASA or SpaceX. The authors would also like to thank Dr. Charles Campbell who served as the Project Manager of the Propulsive Descent Technology project and who provided critical feedback and review of this work.

References

[1] Horvath, T. J., Aubuchon, V. V., Rufer, S. J., Campbell, C. H., Schwartz, R. J., Mercer, C. D., Tack, S., Spisz, T. S., Taylor, J. C., Gibson, D. M., Osei-wusu, K., Kennerly, S., Scriven, G., Pottebaum, T., and Ross, M., "Advancing Supersonic Retro-Propulsion Technology Read-iness: Infrared Observations of the SpaceX Falcon 9 First Stage," *Proceedings of the AIAA SPACE 2017 Conference*, AIAA, 2017.

[2] Dwyer Ciancolo, A. M., Davis, J. L., Engelund, W. C., Komar, D., Queen, E. M., Samareh, J. A., Way, D. W., Zang, T. A., Murch, J. G., Krizan, S. A., et al., "Entry, Descent and Landing Systems Analysis Study: Phase 1," Tech. Rep. TM 216720, NASA, July 2010.

[3] Dwyer Ciancolo, A. M., Davis, J. L., Engelund, W. C., Komar, D., Queen, E. M., Samareh, J. A., Way, D. W., Zang, T. A., Murch, J. G., Krizan, S. A., et al., "Entry, Descent and Landing Systems Analysis Study: Phase 2 Report on Exploration Feed-Forward Systems," Tech. Rep. TM 217055, NASA, February 2011.